Simulation of Semiconductor Processes and Devices 2016
Edited by E. Bär, J. Lorenz, and P. Pichler

Unified Regional Fermi-Potential-Based Compact Model for Double Heterostructure HEMTs

Arjun Ajaykumar*‡, Xing Zhou*§, Siau Ben Chiah*, Binit Syamal*
*School of Electrical and Electronic Engineering, Nanyang Technological University,
50 Nanyang Avenue, Singapore 639798
Email: ‡arjun007@e.ntu.edu.sg;§exzhou@ntu.edu.sg

***Abstract*—Triangular quantum-well (QW) based high electron mobility transistors (HEMTs) and their compact models have been extensively studied in the past. InGaAs-based double heterostructure HEMTs with rectangular-QW confinement are garnering much interest recently. The coupled Poisson-Schrödinger (PS) studies show that triangular-QW compact models are inconsistent with the double heterostructure physics. This paper presents a complete physics-based unified regional Fermi-potential (E_f) model for rectangular QW devices. The E_f along with the derived interface potential solution (E_{if}) are used to capture the complete device electrostatics. The paper also discusses the modeling of $I_d - V_d$ and $I_d - V_g$ characteristics of the device from the Fermi potential.**

I. Introduction

High electron mobility transistors (HEMTs) are heterostructure-based devices with improved mobility and low-noise characteristics. HEMTs based on AlGaN/GaN heterostructures (Fig. 1a) have been studied extensively [1], [2]. These single heterojunction devices use a triangular potential well, as shown in Fig. 1b, for the carrier confinement. Recently, InGaAs-based HEMTs are gaining importance [3], [4]. The schematic of such a device is shown in Fig. 2a. Unlike the single heterojunction devices, InGaAs devices use a double heterostructure for carrier confinement. The lattice matched thin layers used reduces the defect density and improves the carrier confinement [5]. The delta doping allows the possibility of the thinner barrier layer to have better transconductance [5]. The InAs layer inserted into the QW ensures mobility enhancement and further improves the carrier confinement [6].

The coupled Poisson-Schrödinger (PS) Fermi potential solution for the triangular and rectangular QWs differ due to the different nature of carrier confinement [7]. Many compact device models for triangular-QW devices have been developed in the past [8], [9], [10]. It was shown that the existing triangular-QW based compact models fail for rectangular-QW based devices [7]. This paper presents a complete regional Fermi-potential-based compact model, including the charge and IV modeling, for double heterostructure HEMTs. The Fermi potential solutions are used in conjunction with the drift-diffusion (DD) equations to predict the DC characteristics of the device. The model scalability and accuracy are discussed elsewhere [7]. The outline for the paper is as follows. Section II describes the model formulation. Section III presents the results and discussion. Lastly, section IV presents the conclusion.

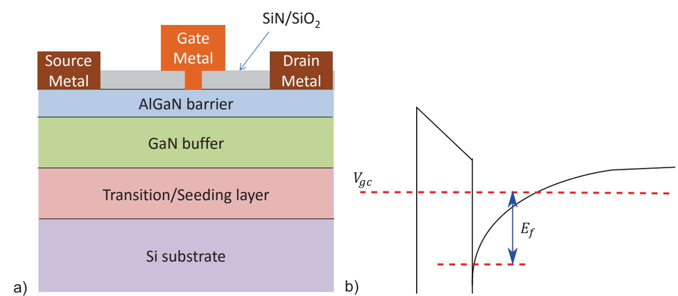

Figure 1. a) The schematic of a GaN-based HEMT with a single heterojunction at AlGaN barrier and GaN buffer interface. b) The band diagram of the device. The carries reside in the low-energy-triangular-notch formed at AlGaN and GaN interface.

II. Model Formulation

Fig. 2b shows the conduction band diagram of the InGaAs HEMT shown in Fig. 2a. $\vec{F}_{ox}$, $\vec{F}_{cap}$, $\vec{F}_{1b}$, $\vec{F}_{2b}$, and $\vec{F}_{wb}$ are the electric fields in oxide, cap, barriers, and QW barrier layers, respectively, whose thicknesses are given as T_{ox}, T_{cap}, T_{b1}, T_{b2}, and T_{wb}. The InAs channel region thickness is given as T_w. The different material electron affinities result in the conduction band offsets at the interfaces of gate metal, oxide, cap, barrier, and QW regions given as Φ_M, Φ_S, ΔE_1, ΔE_2, and ΔE_3, as shown in Fig. 2b. E_0 and E_1 are the quantized energy levels in the rectangular QW. The carriers are confined in the rectangular QW in the InAs region. E_f is the Fermi potential referenced to the bottom of the QW at the interface between the InGaAs barrier and InAs channel. The E_f has the same definition as the surface potential in conventional MOSFETs. According to the applied gate bias, three regions of operation can be identified as sub-threshold where $E_f < E_0$, weak inversion where $E_0 < E_f < E_1$, and strong inversion where $E_f > E_1$. Due to the low band gap in InAs, an accumulation region occurs at very negative voltage bias. The Fermi potential in the sub-threshold regime,

978-1-5090-0818-6/16/$31.00 ©2016 IEEE

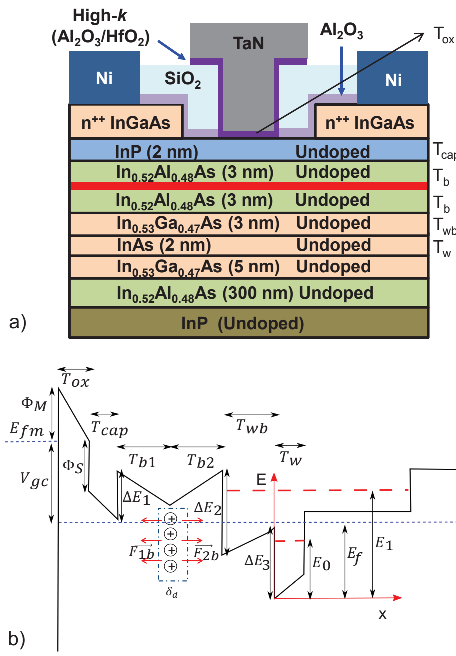

Figure 2. a) The schematic of an InGaAs-based HEMT with double heterojunction formed by InGaAs at the left and right interfaces of InAs. b) The detailed band diagram and electric fields in the device. The carriers supplied by the δ_d doping reside in the low-energy rectangular-QW region and forms the conducting channel.

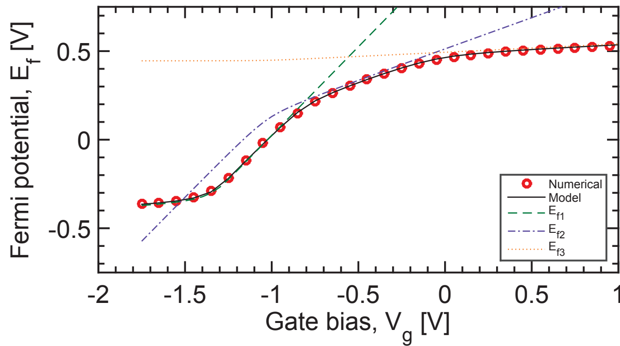

Figure 3. Unified Fermi-potential (E_f) model comparison with numerical data extracted from the coupled Poisson-Schrödinger (PS) simulation. The regional models (E_{f1}, E_{f2}, and E_{f3}) are combined using a smoothing function given by (7).

including the accumulation region, is given as

$$E_{f1} = V_{gc} - V_{off} + \frac{kT}{q} W \left\{ \frac{q^2 N_v T_w e^{\frac{-qE_g}{kT}}}{kTC_d} e^{\frac{-q\left(V_{gc}-V_{off}\right)}{kT}} \right\} \tag{1}$$

where W is the Lamberts W function, E_g and N_v are the band gap and effective density of states in the valence band, respectively. V_{off} and C_d are the off voltage and effective gate capacitance, respectively.

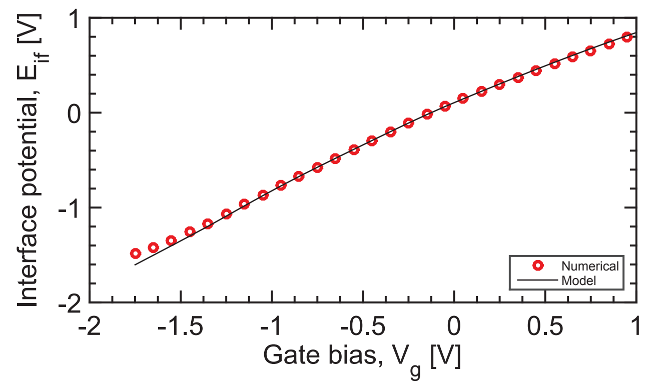

Figure 4. Fermi interface potential model, governed by (8), comparison with numerical data extracted from the coupled Poisson-Schrödinger (PS) simulation.

The weak-inversion piece is given as [7]

$$E_{f2} = \frac{V_{gc} - V_{off} + \frac{qD_w E_0}{C_d}}{1 + \frac{qD_w}{C_d}} \tag{2}$$

The strong-inversion piece is given as [7]

$$E_{f3} = \frac{-B + \sqrt{B^2 - 4AC}}{2A} \tag{3}$$

$$A = D_w \frac{\Omega^2}{8} \frac{m_w^* q^3 {D_{wb}}^2 T_w^4}{{\epsilon_{wb}}^2 \hbar^2} \tag{4}$$

$$B = 2D_w + 2D_{wb} + D_b + D_{cap} + \frac{C_d}{q} - 2E_1 A \tag{5}$$

$$C = AE_1^2 - (D_w + 2D_{wb} + D_{cap} + D_b)E_1 - D_w E_0 - \frac{C_d}{q}(V_{gc} - V_{off}) \tag{6}$$

The unified regional E_f is given as [7]

$$E_f = \vartheta(E_{f3}, E_{fSW}; \delta_{str}) \tag{7}$$

where $E_{fSW} = \vartheta(E_{f0}, E_{f1}^{'}; \delta_{sub})$ and δ_s, δ_{sub}, and δ_{str} are the smoothing parameters. Table I summarizes the other

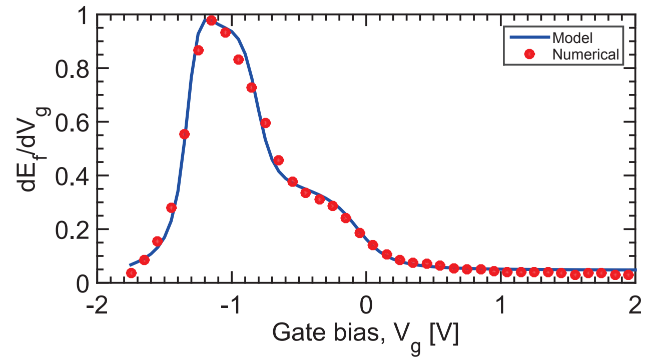

Figure 5. The first derivative of E_f shows no abrupt discontinuities indicating a smooth transition between different operating regimes.

relevant model equations. For high gate bias, the carriers spill

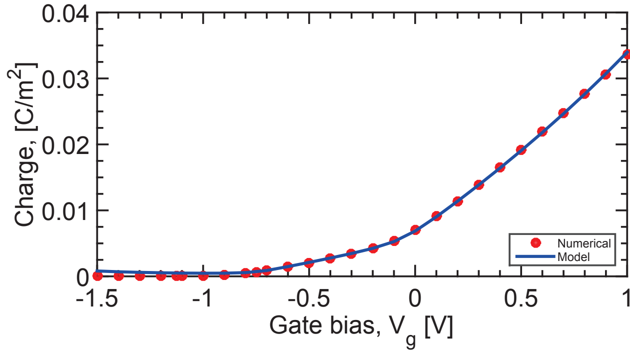

Figure 6. Model accurately matches the charge variation with gate bias extracted from numerical simulations. The charge variation is governed by (9).

over from the rectangular-QW confinement, resulting in a parallel-channel formation. The Fermi potential and potential at the interface of oxide and parallel channel, E_{if}, are used to model the charge and current accurately. E_{if} is given as

$$E_{if} = V_{gc} - V_{off,pc} + V_{ox} \tag{8}$$

The terminal-bias dependency on the total gate charge is given as

$$Q_g = Q_{C,V_{dc}} + Q_{PC,V_{dc}} + q\upsilon_\delta \delta E_0^2 \delta_d \tag{9}$$

where

$$Q_{C,V_{dc}} = C_d \left(V_{gc} - V_{off} - E_{f,V_{dc}}\right)$$

and $Q_{PC,V_d} = C_{ox}\left(V_{gc} - V_{off,pc} - E_{if,V_{dc}}\right)$ are the bias dependent charge in the channel and parallel channel governed by E_f and E_{if}, respectively.

The υ_{Ef}, υ_{Eif}, and υ_δ are fitting parameter to capture the electric field screening due to the spilled carriers at high V_{gc} compared to the low V_{gc} case. The unified Fermi-potential solution is used with the conventional DD equations to simulate the device DC characteristics [9], [11].

$$I_d = \mu_{eff} C_d \frac{W}{L}\left[V_g - V_{off} - \overline{E_f} + 2\frac{kT}{q}\right] V_{dseff} \tag{10}$$

where μ_{eff} and $\overline{E_f} = \left(2E_f + V_{seff} + V_{deff}\right)/2$ are the effective mobility and average E_f, respectively.

This formalism uses ground referencing and hence ensures Gummel symmetry. The model also incorporates the short channel effects like drain-induced barrier lowering (DIBL) and the channel-length modulation (CLM). The change in the sub-threshold slope of $I_d - V_g$ with drain bias is captured by modifying the V_{off} according to the quasi-2D surface potential shift discussed in [9], [11], [12]. Table II summarizes the material and physical parameters used.

III. Results and Discussion

Fig. 3 shows the regional and unified Fermi-potential variations with gate bias. The sub-threshold regional piece, E_{f1}, saturates at higher negative bias because of the accumulation region arising due to low band gap $(0.33eV)$ of the InAs channel. The unified model, E_f, matches the numerical solution obtained from the coupled PS solution accurately.

Table I
Model equations

$$V_{off} = \Phi_M - \Phi_S + \Delta E_1 - \Delta E_2 - \Delta E_3 - \frac{qT_{ox}\delta_d}{\epsilon_{ox}} - \frac{qT_{cap}\delta_d}{\epsilon_{cap}} - \frac{qT_{b1}\delta_d}{\epsilon_b}$$

$$V_{off,pc} = (\Phi_M - \Phi_S)$$

$$V_{go,eff} = 0.5\left(V_{gc} - V_{off} + \sqrt{(V_{gc} - V_{off})^2 + 4\delta_s}\right)$$

$$C_d = \frac{1}{\frac{T_{ox}}{\epsilon_{ox}} + \frac{T_{cap}}{\epsilon_{cap}} + \frac{T_{b1}}{\epsilon_b} + \frac{T_{b2}}{\epsilon_b} + \frac{T_{wb}}{\epsilon_{wb}}}$$

$$C_{ox} = \frac{\epsilon_{ox}}{T_{ox}}$$

$$V_{ox} = \frac{q\delta_d - C_d\left(V_{go,eff} - E_f\right)}{C_{ox}}$$

$$\delta E_0 = -\frac{\Omega^2}{8}\frac{m_w^* q F^2 T_w^4}{\hbar^2}$$

$$\Omega = P\Big[\frac{1}{3} + \frac{\sin k_0}{k_0} + \frac{2\cos k_0}{k_0^2} - \frac{2\sin k_0}{k_0^3} + \frac{2}{q_0}\left[1 + \frac{2}{q_0} + \frac{2}{q_0^2}\right]\cos^2\frac{k_0}{2}\Big]$$

$$F = \frac{qD_{wb}(E_f - E_1)}{\epsilon_{wb}}$$

$$P = \left[1 + \frac{\sin k_0}{k_0} + \frac{2}{q_0}\cos^2\frac{k_0}{2}\right]^{-1}$$

$$k_0^2 = \frac{2m_w^* T_w^2 q}{\hbar^2} E_0$$

$$q_0^2 = \frac{2m_w^* T_w^2 q}{\hbar^2}(U_0 - E_0)$$

$$U_0 = \Delta E_3$$

$$\vartheta(x, y; \alpha) = 0.5\left(x + y + \alpha - \sqrt{(x - y - \alpha)^2 + 4\alpha x}\right)$$

$$E_{f1}' = E_{f1}|_{V_{gc} - V_{off} = V_{go,eff}}$$

$$E_{f,V_{dc}} = E_f + \upsilon_{Ef}\delta E_0 + \zeta V_{dc}$$

$$E_{if,V_{dc}} = E_{if} + \upsilon_{Eif}\delta E_0 + \zeta V_{dc}$$

$$V_{dseff} = V_{deff} - V_{seff}$$

$$V_{deff} = \vartheta(V_{dsat}, V_d; \alpha)$$

$$V_{seff} = \vartheta(V_{ssat}, V_d; \alpha)$$

Table II
Materials and Physical Parameters

Oxide	-	HfO_2
Cap	-	InP
Barrier	-	$In_{0.52}Al_{0.48}As$
Well Barrier	-	$In_{0.53}Ga_{0.47}As$
Well	-	InAs
δ_d	cm^{-2}	5×10^{12}
T_{ox}	nm	2
T_{cap}	nm	2
T_b	nm	3
T_{wb}	nm	3
T_w	nm	2
E_0	V	0.213
E_1	V	0.49V
D_{cap}	$m^{-2}V^{-1}$	3.316×10^{17}
D_b	$m^{-2}V^{-1}$	3.57×10^{17}
D_{wb}	$m^{-2}V^{-1}$	1.37×10^{17}
D_w	$m^{-2}V^{-1}$	1.08×10^{17}

Fig. 4 shows the E_{if} variation with gate bias, captured by calculating the relative variation of E_f at the interface of the oxide and parallel channel. The model predicts the coupled PS simulation accurately. The derivative of E_f (Fig. 5) shows no abrupt discontinuities, indicating smooth interoperating regime transitions.

Figs. 6 and 7 demonstrate the comparison between model and numerical solution for charge and capacitance (dQ_g/dV_g) variation, respectively, with terminal biases. The model matches numerical simulation data thus capturing the device electrostatics accurately. Figs. 8 and 9 show a comparison of

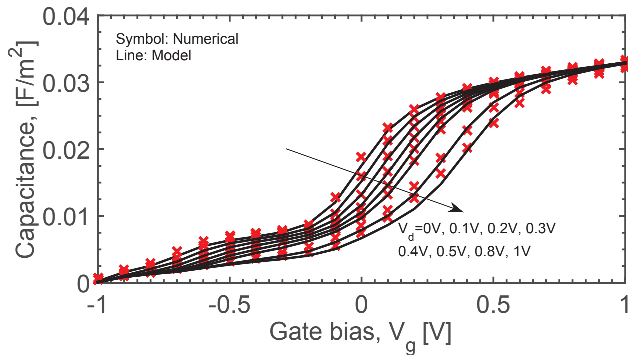

Figure 7. The model predicts capacitance (dQ_g/dV_g) variation with drain bias thus accurately capturing the electrostatics of the device.

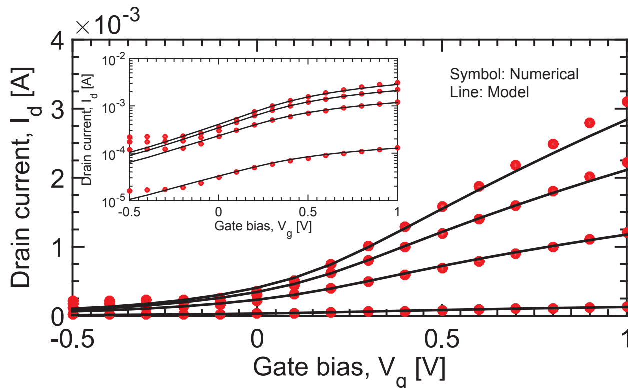

Figure 8. The model matches the $I_d - V_g$ characteristics of an InGaAs HEMT with channel length (L) and width (W) of 500nm and 1μm accurately. The drain voltages applied are $0.01V$, $0.1V$, $0.2V$, and $0.3V$.

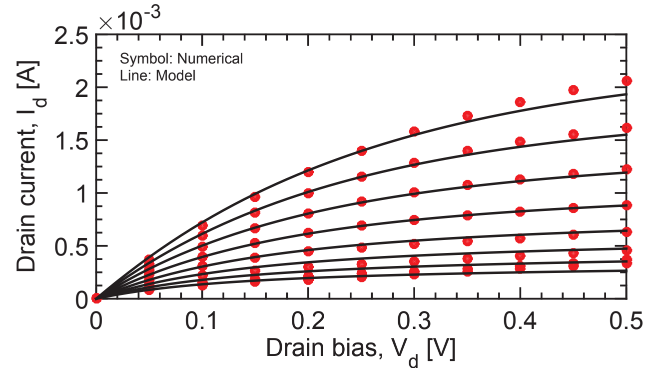

Figure 9. The model matches $I_d - V_d$ characteristics of an InGaAs HEMT with channel length (L) and width (W) of 500nm and 1μm accurately. The gate voltage is varied from $-0.2V$ to $0.5V$ with a step size of $0.1V$. The short-channel effects like DIBL and CLM are incorporated into the E_f model as discussed in [9], [11], [12].

the model with numerical $I_d - V_d$ and $I_d - V_g$ of an InGaAs HEMT with channel length of 500nm and width of 1μm. The complete unified model incorporated with the DIBL and CLM captures the DC characteristics accurately.

IV. Conclusion

This paper presents a complete unified regional Fermi-potential model for double heterostructure HEMTs with rectangular quantum well. The new model is scalable and captures the device physics more accurately than the existing triangular-quantum-well based compact models. The model is used in conjunction with the DD equations to simulate the device DC characteristics.

Acknowledgment

This work was supported in part by the National Research Foundation, Prime Ministers Office, Singapore through the Singapore MIT Alliance for Research and Technologys Low Energy Electronic Systems research program SMART-LEES Subawards 16 and 23.

References

[1] T. J. Anderson, M. J. Tadjer, J. K. Hite, J. D. Greenlee, A. D. Koehler, K. D. Hobart, and F. J. Kub, "Effect of reduced extended defect density in mocvd grown AlGaN/GaN hemts on native gan substrates," *IEEE Electron Device Lett.*, vol. 37, no. 1, pp. 28–30, Jan 2016. DOI: 10.1109/LED.2015.2502221.

[2] Y. Cai, Y. Zhou, K. J. Chen, and K. M. Lau, "High-performance enhancement-mode AlGaN/GaN hemts using fluoride-based plasma treatment," *IEEE Electron Device Lett.*, vol. 26, no. 7, pp. 435–437, July 2005. DOI: 10.1109/LED.2005.851122.

[3] J. A. del Alamo, D. A. Antoniadis, J. Lin, W. Lu, A. Vardi, and X. Zhao, "III-V MOSFETs for Future CMOS," in *Compound Semiconductor Integrated Circuit Symposium (CSICS), 2015 IEEE*, Oct 2015, pp. 1–4. DOI: 10.1109/CSICS.2015.7 314 512.

[4] J. Lin, D. A. Antoniadis, and J. A. del Alamo, "Impact of Intrinsic Channel Scaling on InGaAs Quantum-Well MOSFETs," *IEEE Trans. Electron Devices*, vol. 62, no. 11, pp. 3470–3476, Nov 2015. DOI: 10.1109/TED.2015.2444835.

[5] D. Fritzsche, "Heterostructures in MODFETs," *Solid-State Electronics*, vol. 30, no. 11, pp. 1183 – 1195, 1987. DOI: http://dx.doi.org/10.1016/0038-1101(87)90085-2. [Online]. Available: http://www.sciencedirect.com/science/article/pii/0038110187900852

[6] T. Akazaki, K. Arai, T. Enoki, and Y. Ishii, "Improved InAlAs/InGaAs HEMT characteristics by inserting an InAs layer into the InGaAs channel," *IEEE Electron Device Lett.*, vol. 13, no. 6, pp. 325–327, June 1992. DOI: 10.1109/55.145073.

[7] A. Ajaykumar, X. Zhou, B. Syamal, and S. B. Chiah, "Compact Fermi Potential Model for Heterostructure HEMTs With Rectangular Quantum Well," in *Solid State Device Research Conference (ESSDERC), 2014 44th European*, Sept 2014, pp. 266–269. DOI: 10.1109/ESS-DERC.2014.6 948 811.

[8] J. Zhang, B. Syamal, X. Zhou, S. Arulkumaran, and G. I. Ng, "A Compact Model for Generic MIS-HEMTs Based on the Unified 2DEG Density Expression," *IEEE Trans. Electron Devices*, vol. 61, no. 2, pp. 314–323, Feb 2014. DOI: 10.1109/TED.2013.2295400.

[9] B. Syamal, X. Zhou, S. B. Chiah, A. M. Jesudas, S. Arulkumaran, and G. I. Ng, "A comprehensive compact model for GaN HEMTs, including quasi-steady-state and transient trap-charge effects," *IEEE Trans. Electron Devices*, vol. 63, no. 4, pp. 1478–1485, April 2016. DOI: 10.1109/TED.2016.2533165.

[10] M. Li and Y. Wang, "2-D analytical model for current-voltage characteristics and transconductance of AlGaN/GaN MODFETs," *IEEE Trans. Electron Devices*, vol. 55, no. 1, pp. 261–267, Jan 2008. DOI: 10.1109/TED.2007.911076.

[11] X. Zhou, G. Zhu, G. See, K. Chandrasekaran, S. Chiah, and K. Lim, "Unification of MOS compact models with the unified regional modeling approach," *Journal of Computational Electronics*, vol. 10, no. 1-2, pp. 121–135, 2011. [Online]. Available: http://dx.doi.org/10.1007/s10825-011-0354-y

[12] B. Syamal, S. B. Chiah, X. Zhou, A. Ajaykumar, M. J. Anand, G. I. Ng, and S. Arulkumaran, "GaN HEMT compact model for circuit simulation," in *Electron Devices and Solid-State Circuits (EDSSC), 2015 IEEE International Conference on*, June 2015, pp. 535–538. DOI: 10.1109/EDSSC.2015.7 285 169.